RSC Advances

PAPER

View Article Online
View Journal | View Issue

Cite this: *RSC Adv.*, 2026, **16**, 10100

Development of dual acting selenium-doped hydroxyapatite nanoparticles with platinum-bisphosphonate complexes for bone cancer therapy

Alessandra Barbanente,[a] Anna Maria Di Cosola,[a] Federica Rizzi,[bc] Nicoletta Depalo,[bc] Roberto Comparelli,[bc] Rachele Castaldo,[d] Elisabetta Fanizza,[abc] Paride Papadia,[e] Concetta Pacifico,[a] Mauro Niso[f] and Nicola Margiotta *[a]

Bone represents one of the most common sites for metastasis originating from solid tumors, especially breast and prostate cancers, causing severe complications like pain, fractures, and impaired quality of life. Hydroxyapatite (HA) nanoparticles (NPs) have been considered as good candidates for bone-targeted drug delivery due to their biocompatibility and osteoconductivity. In this study, we developed selenium-doped hydroxyapatite (HASe) NPs with reduced selenium content (up to 2.40 wt%) with the aim of overcoming the toxicity issues associated with previously reported higher Se doping levels. The HA-based NPs were thoroughly characterized to evaluate their morphological, colloidal, and compositional features, supporting the effective incorporation of selenium (Se) within the HA structure. *In vitro* cytotoxicity assays on MCF7wt breast cancer cells demonstrated a clear Se dose-dependent reduction in viability. To improve the anticancer potential, HA and selected HASe NPs were further functionalized with two HA-binding anti-tumor platinum-bisphosphonate (PtBP) complexes. The resulting PtBP-HASe NPs exhibited stronger cytotoxicity than PtBP-HA, despite their lower platinum content, highlighting an additional effect due to the presence of Se. Notably, PtBP-HASe NPs maintained a cytotoxic profile comparable to more highly doped HASe formulations, while reducing their Se content, potentially improving safety. Mechanistic investigations confirmed that reactive oxygen species (ROS) contribute to the antiproliferative activity of both the platinum complexes and the functionalized NPs, providing insight into the redox-mediated cytotoxicity of these nanomaterials. These findings suggest that PtBP-HASe NPs represent a promising dual-action biomaterial for bone-targeted cancer therapy, combining anticancer efficacy with enhanced biocompatibility potential.

Received 3rd December 2025
Accepted 13th February 2026

DOI: 10.1039/d5ra09348a

rsc.li/rsc-advances

Introduction

Bone is a common site for metastases derived from non-osseous tumors. In fact, many common cancers, in particular breast and prostate, have a strong predilection to metastasize to bones.[1] Bone metastases lead to severe complications, including pain, hypercalcemia, skeletal fractures, and spinal instability, significantly reducing patients' quality of life. Bone tumors or metastases develop through a "vicious cycle" whereby tumor cells disrupt the physiological balance between osteoblast-driven bone formation and osteoclast-mediated bone resorption, while simultaneously exploiting several growth factors released from the extracellular bone matrix to support their own proliferation and survival.[2,3] Current treatment strategies for bone tumors include surgery, chemotherapy, radiotherapy, bisphosphonates and analgesics.[4,5] However, surgical resection is often not affordable for patients with limited life expectancy, as residual tumor cells may persist, and large bone defects require additional interventions for repair.[6] A promising alternative approach for bone cancer therapy lies in the design of multifunctional biomaterials capable of simultaneously supporting bone regeneration and inhibiting tumor growth. Among these,

[a]*Department of Chemistry, University of Bari Aldo Moro, via E. Orabona 4, 70126 Bari, Italy. E-mail: nicola.margiotta@uniba.it*
[b]*Institute for Chemical and Physical Processes (IPCF)-CNR SS Bari, via Orabona 4, Bari, 70126, Italy*
[c]*National Interuniversity Consortium of Materials Science and Technology (INSTM), Bari Research Unit, 70126 Bari, Italy*
[d]*Institute of Polymers, Composites and Biomaterials (IPCB)-CNR, via Campi Flegrei 34, 80078 Pozzuoli, Naples, Italy*
[e]*Department of Biological and Environmental Sciences and Technologies (DiSTeBA), University of Salento, 73100 Lecce, Italy*
[f]*Department of Pharmacy-Pharmaceutical Sciences, University of Bari Aldo Moro, via Orabona 4, 70126 Bari, Italy*

calcium phosphate-based materials have received increasing attention owing to their close chemical affinity with the mineral phase of bone and their dual capacity to provide structural support and therapeutic functionality. In particular, hydroxyapatite (HA) nanoparticles (NPs) have emerged as multifunctional nanoplatforms[7–11] due to their unique structural and biological features.[12–14] Indeed, HA, being the main inorganic component of bone, exhibits excellent biocompatibility, osteoconductivity, and intrinsic bioactivity, which makes it particularly suitable for applications in bone-related diseases.[15] Moreover, tunable physico-chemical features of HA NPs, including size, morphology, porosity and crystallinity and surface functionality,[16] enable high drug-loading efficiency and controlled and sustained release of chemotherapeutic agents.[17] The chemical similarity of HA to native bone mineral promotes strong interactions with the bone matrix, ensuring site-specific accumulation and prolonged local drug retention, thus representing an ideal bone substitute for implantable devices designed to deliver bioactive molecules while promoting tissue regeneration.[18]

The biological performance of HA can be further enhanced through doping with trace ions of elements such as magnesium,[19] strontium,[20] and zinc,[21] which improve osteogenesis and reduce inflammation. Selenium (Se) is a particularly interesting dopant due to its unique role in human health and disease being involved in many physiological processes such as growth, metabolism, and hormone balance. Se has also shown antitumoral activity through apoptosis, necrosis, or regulation of redox state.[22] Among its inorganic forms, selenite ion (SeO_3^{2-}) is the most studied species due to its excellent chemo preventive and anticancer properties.[23] Selenite ions effectively inhibit the proliferation of multiple cancer cell types[24] and play a role in natural killer (NK) cell-based anticancer immunotherapy, by increasing tumor cell susceptibility to CD94/NK group 2A-positive NK cells.[25] Furthermore, hydrogen selenide (H_2Se), a key intermediate generated during the metabolic reduction of dietary selenite, has been shown to induce apoptosis in cancer cells (HepG2, HeLa, and MCF-7) through mitochondrial accumulation. This selenite-induced accumulation impairs mitochondrial function and structure, ultimately triggering cancer cell death.[26]

Given these promising anticancer properties, selenium-doped hydroxyapatite (HASe) has been explored for its antibacterial, anticancer, and osteoinductive capabilities.[27–31] Very recently, some of co-authors reported the synthesis of HASe nanoparticles (HASe NPs) with Se concentration ranging from 0.4 to 13.2 %wt, which were tested on prostate and breast cancer cells (PC3 and MDA-MB-231, respectively), as well as on human bone marrow-derived stem cells (hBMSCs).[32] The *in vitro* studies revealed a clear concentration-dependent effect: HASe NPs with a very low Se concentration (0.4 %wt) exhibited good biocompatibility but lacked significant anticancer activity, whereas NPs with higher Se concentrations displayed strong cytotoxicity against cancer cells but also increased toxicity toward healthy hBMSCs. These results indicated that careful tuning of Se concentration is crucial to maximize anticancer efficacy while maintaining biocompatibility.

Given this balance between efficacy and safety, combination chemotherapy represents a promising strategy to enhance treatment outcomes. In particular, selenite ions have been shown to potentiate the effect of various chemotherapeutic agents, including camptothecin, 5-fluorouracil (5-FU), oxaliplatin, irinotecan, and docetaxel, by increasing their cytotoxic effects on cancer cells while potentially reducing systemic toxicity.[33,34] Additionally, selenite has also been used in combination with platinum (Pt)-based drugs to mitigate nephrotoxicity and bone marrow suppression by forming Se–Pt complexes, which reduce Pt toxicity while maintaining its therapeutic activity.[35,36] However, the precise mechanism underlying the protective role of Se remains largely unclear. Zeng *et al.* demonstrated that Se and Pt, when combined into aggregates (that they called EG-Se/Pt), could selectively eliminate liver carcinoma cells through reactive oxygen species (ROS)-induced apoptosis, while exhibiting lower toxicity toward healthy liver cells.[37,38] Very recently, some of us reported the development of HASe NPs functionalized by the adsorption of a Pt-pyrophosphate (PtPP) complex, resulting in PtPP-HASe NPs. In particular, experiments using combined Pt and Se releasates from the PtPP-HASe NPs at different Pt/Se ratios (2, 4, and 8) revealed that a Pt/Se ratio of 8 significantly inhibited the proliferation of cancer cells co-cultured with hBMSCs.[39]

Building on previous findings that highlighted the potential of Se-doped HA NPs, particularly in combination with Pt-based complexes for anticancer applications, this study aims to further refine and optimize these materials to maximize therapeutic efficacy while minimizing toxicity. Specifically, we synthesized HA NPs and HASe NPs with lower Se content (HASe2.5%, HASe5.0% and HASe7.5%; the number in the label of the NPs indicates the nominal Se/(Se + P) molar ratio, based on the initial reagent feed composition) to address the cytotoxicity concerns associated with the higher Se concentrations used in previous works.[32] Here, a comprehensive physico-chemical characterization of the synthesized Se-doped HA NPs was carried out to identify the most promising candidate in terms of biocompatibility and Se induced-anticancer activity. Based on these results, selected HA and HASe5.0% NPs were then loaded with two pharmacologically active platinum-bisphosphonate complexes, namely $[\{Pt(1R,2R\text{-DACH})\}_2(ZL)]NO_3$ (PtBP1; DACH = diaminocyclohexane, ZL = zoledronate; see Fig. 3 for the chemical structure) and $[\{Pt(cis\text{-}1,4\text{-DACH})\}_2(ZL)]NO_3$ (PtBP2), with the aim of investigating their potential as dual-action bone-targeting biomaterials.[40] Remarkably, given the challenges associated with high Se concentrations, our approach aims to achieve an optimal balance between therapeutic efficacy and biocompatibility. As a preliminary pharmacological evaluation, the cytotoxic activity of HASe NPs suspensions was assessed in direct treatment of breast cancer cells (MCF-7 wt). To further elucidate the mechanisms underlying their antiproliferative effects, the involvement of reactive oxygen species (ROS) was also investigated, laying the groundwork for a more comprehensive understanding of their biocompatibility and therapeutic potential.

Experimental

Materials and methods

Chemicals. High-purity chemical reagents such as calcium acetate hydrate ($Ca(CH_3COO)_2$, >99%), orthophosphoric acid

($H_3PO_4 \geq 85\%$ wt in water), sodium selenite (Na_2SeO_3, ≥98%), ammonium hydroxide ($(NH_4)OH$, ≥ 30% wt in water), ultrapure nitric acid for Inductively Coupled Plasma Atomic Emission Spectroscopy (ICP-AES) analysis (HNO_3, ≥70% wt in water), MTT (3-[4,5-dimethylthiazol-2-yl]-2,5-diphenyltetrazoliumbromide) were purchased from Sigma Aldrich (Milan, Italy). All cell culture reagents were purchased from S.I.A.L. S.r.l. (Rome, Italy).

Synthesis of HASe NPs. HASe NPs were prepared according a method already reported.[32] Briefly, selenium – in the form of selenite anions – was incorporated into HA NPs by precipitation from an aqueous solution of H_3PO_4 and Na_2SeO_3 by the slow addition (1 drop per s) of an aqueous solution of $Ca(CH_3COO)_2$. The reaction was carried out at pH = 9 by adding few mL of 15% wt $(NH_4)OH$ solution to the phosphate solution. Se-free stoichiometric HA NPs ($Ca_5(PO_4)_3OH$) were produced, as reference material, with the same method without adding the Se source to the phosphoric acid solution. In this latter case, 83 mM $Ca(CH_3COO)_2$ and 50 mM H_3PO_4 solutions were used. The reaction mixtures were kept under magnetic stirring at room temperature for 24 h, then left standing for about 30 min without stirring to allow the deposition of the inorganic phase. This latter was isolated by centrifugation (Thermo Scientific centrifuge, T = 25 °C, 4500 rpm for 5 min) of the reaction mixture, repeatedly washed with Milli-Q® water, and freeze-dried at −50 °C overnight. HASe NPs were synthesized by using different Na_2SeO_3 concentration as a function of the calculated substitution percentage and adjusting the calcium and phosphorous molarity. The amounts of reagents were calculated with the assumption that one orthophosphate ion is replaced by one selenite ion with a concurrent loss of one calcium ion, and the reagent were used in the opportune quantities to yield a Ca/(P + Se) molar ratio of 1.635, 1.61, and 1.585 corresponding, respectively, to a Se/(P + Se) molar ratio of 0.025 (HASe2.5%), 0.05 (HASe5.0%), and 0.075 (HASe7.5%). The detailed experimental parameters are summarized in Table 1.

Preparation and characterization of [{Pt(1*R*,2*R*-DACH)}$_2$(ZL)]NO_3 (PtBP1; DACH = diaminocyclohexane, ZL = zoledronate) and [{Pt(*cis*-1,4-DACH)}$_2$(ZL)]NO_3 (PtBP2). 1-Hydroxy-3-(1*H*-imidazole-1-yl)ethane-1,1-diylbisphosphonic acid (zoledronic acid, ZL), was prepared following a previously reported procedure.[40] [{Pt(1*R*,2*R*-DACH)}$_2$(ZL)]NO_3 and [{Pt(*cis*-1,4-DACH)}$_2$(ZL)]NO_3 (see Fig. 3 for Pt-complexes' structures) were prepared as described in earlier studies.[41] Spectroscopic and spectrometric analyses confirmed that the synthesized compounds were consistent with the reported data.

Loading of HA and HASe5% NPs with PtBP1 and PtBP2. PtBP1 and PtBP2 were loaded into lyophilized HA and HASe5% NPs according to a method already reported.[39] Briefly, HA or HASe5.0% NPs were suspended in water at a concentration of 6.67 mg mL^{-1} (30 mg HA or HASe5.0% NPs in 4.5 mL H_2O) in a 15 mL Falcon tube, to which 4.5 mg of PtBP1 or PtBP2 were added to achieve a 1.0 mg mL^{-1} concentration. The Falcon tubes were then vortexed for 15 s, after which the suspensions were maintained in a bascule bath at 37 °C shaking at 60 rpm for 24 h. Subsequently, the suspensions underwent centrifugation (5 min at 5000 rpm). After supernatant removal, PtBP1-HA, PtBP2-HA, PtBP1-HASe5.0%, and PtBP2-HASe5.0% NPs were washed twice using ultrapure water to remove the unloaded Pt(II) complexes. The total amount of Pt and Se residual after loading of PtBP1 and PtBP2 into HA and HASe5.0% NPs was quantified by dissolving 1 mg of PtBP1-HA, PtBP2-HA, PtBP1-HASe5.0%, and PtBP2-HASe5.0% NPs in 65 vol% nitric acid. After complete dissolution, the solutions were diluted with Milli-Q water to obtain 1 vol% nitric acid. Additionally, 4 mL of the supernatants collected after the loading process were acidified to 1 vol% nitric acid by dilution with Milli-Q water. All the solutions were analyzed for measuring Pt and Se concentration by ICP-AES (Thermo iCAP 6000 spectrometer). The values are presented as mean ± standard deviation (n = 3).

The encapsulation efficiency (EE%) was calculated using the following equation:

$$EE\% = (W_t/W_i) \times 100$$

where W_t is the amount of platinum effectively loaded into the HA and HASe5% NPs, and W_i is the initial amount of platinum used in the loading process.

Physicochemical characterization of HA-based NPs. Transmission electron microscopy (TEM) characterization was performed by using a JEM1011 instrument (JEOL, Akishima, Tokyo, Japan) that works at 100 keV, equipped with a high-resolution CCD camera. The carbon-coated copper grids were used for the deposition of the samples in EtOH, that was let to evaporate.

Field emission scanning electron microscopy (FE-SEM) was performed using a Zeiss (Oberkochen, Germany) Sigma microscope operating in the range of 0.5–20 kV and equipped with an in-lens secondary electron detector and an INCA energy-dispersive spectroscopy (EDS) detector. The spray-dried samples were mounted onto stainless steel sample holders using double-sided carbon tape and grounded by silver paste. A uniform gold (Au) coating, a few nanometers thick, was deposited onto the samples mounted on silicon chips using a turbomolecular-pumped SC7620 Mini Sputter/Glow Discharge System (Quorum Technologies). FE-SEM analyses were conducted at a constant accelerating voltage (EHT) of 5.00 kV and

Table 1 Reagent amounts used in the preparation of HASe NPs. The percentage in the label of the samples indicates the Se/(Se + P) molar ratio

Sample	$Ca(CH_3COO)_2$ (mmol)	H_3PO_4 (mmol)	Na_2SeO_3 (mmol)	Ca/(P + Se)
HA	8.3	5	0	1.66
HASe2.5%	8.175	4.875	0.125	1.635
HASe5.0%	8.05	4.75	0.25	1.61
HASe7.5%	7.925	4.625	0.375	1.585

a working distance (WD) of 5.0 mm. The micrographs presented are representative images selected from a set of FE-SEM images acquired for each sample, which were obtained from three independent experimental replicates and repeated measurements on the same specimens.

Zetasizer nano ZSP (Malvern, Worcestershire, UK) equipped a 50 mW laser diode emitting at 532 nm, was employed to evaluate the mean hydrodynamic diameter (size), polydispersity index (PDI) and ζ-potential values of the NPs, after sample dilution (1 : 100 in ethanol), as previously reported.[42] Data are referred to as mean ± standard deviation ($n = 3$ replicates).

FTIR characterization was carried out by using a 670 FTIR spectrometer (Varian, Palo Alto, CA, USA) equipped with a diamond ATR accessory of 2 mm and a deuterated tryglicine sulfate (DTGS) detector. A few amounts of each dried sample were put on the internal reflection element and spectra were recorded in the range 4000–400 cm^{-1} acquiring 16 scans with a nominal resolution of 1 cm^{-1}.

Nitrogen adsorption analysis was performed on HA NPs to evaluate the textural properties of the nanoparticles. Brunauer–Emmett–Teller (BET) specific surface area was evaluated by N_2 adsorption at 77 K through a Micromeritics 3Flex analyzer (Norcross, GA, USA). Pore size distribution was evaluated using the Nonlocal Density Functional Theory (NLDFT) analysis. The adsorption measurements were performed using high purity gases (>99.999%). HA NPs were degassed at 150 °C under vacuum before analysis ($P < 10^{-7}$ mbar).

Cell culture. Human breast adenocarcinoma (MCF7wt) cells were obtained from American Type Culture Collection (ATCC, Bethesda, Rockville, MD, USA). MCF7 were cultured in Dulbecco's Modified Eagle's Medium. This medium was supplemented with 10% (v/v) fetal bovine serum, 1% (v/v) glutamine, and 1% (v/v) penicillin–streptomycin. Cells were cultivated at 37 °C with 5% CO_2 at saturated humidity.

***In vitro* cell viability.** The number of living cells was evaluated by the 3-(4,5-dimethylthiazol-2-yl)-2,5-diphenyltetrazolium bromide (MTT) assay. Cells were seeded at a density of 10 000 cells per well into 96-well flat bottom culture plates containing 50 μL of the test samples (ranged from 0.025 mg mL^{-1} to 0.2 mg mL^{-1} final concentration) in a final volume of 100 μL. Untreated cells were used as positive controls. After 72 h of incubation at 37 °C in a 5% CO_2 atmosphere, MTT was added to a final concentration of 0.5 mg mL^{-1} for further 3–4 h, then the culture medium was removed, and the insoluble precipitate was dissolved by the addition of 100 μL of solvent (1 : 1 v/v DMSO/EtOH). The absorbance of each well was measured at 570 nm using a PerkinElmer Victor V3 plate reader. Cell growth inhibition was then calculated as a percentage of cell viability relative to the control and EC_{50} values were determined from dose–response curves by applying a non-linear regression model using GraphPad PRISM version 5.0.

Oxidative stress. ROS involvement in the antiproliferative activity was tested on MCF7wt cells for PtBP1, PtBP2, Na_2SeO_3, HA, PtBP1-HA, PtBP2-HA, HASe5.0%, PtBP1-HASe5%, and PtBP2-HASe5%. In particular, the interference of ROS in cell viability was indirectly determined after 48 h treatment by MTT assay as reported above. On day 1, 25 000 cells per well were seeded into 96-well plates in the presence or absence of α-tocopherol (100 μM). On day 2, the samples (1–100 μM for PtBP1, PtBP2, Na_2SeO_3 and 0.05, 0.1 and 0.2 mg mL^{-1} for HA, HASe5.0%, PtBP1-HA, PtBP2-HA, PtBP1-HASe5.0%, and PtBP2-HASe5.0%) were added alone and in combination with α-tocopherol (100 μM). After incubation (48 h) with samples, MTT (0.5 mg mL^{-1}) was added to each well, and after 3–4 h incubation at 37 °C, the supernatant was removed. The formazan crystals were solubilized with 100 μL DMSO/EtOH (1 : 1), and the absorbance values at λ 570 and 630 nm were determined on a microplate reader Victor 3.

Statistical analysis. Data were analyzed by one-way ANOVA for repeated measures followed by post-hoc Bonferroni's multiple comparison test. Results are expressed as mean ± SD of at 2–3 independent experiments in triplicates. Statistical significance was accepted at a level of $P < 0.05$.

Results and discussion

Synthesis and characterization of HA and HASe NPs

Several emerging nanocarriers are designed for active tumor targeting, often incorporating complex biomimetic, stimuli-responsive, or multi-modal functionalities. For example, platelet-based magnetically guided nanoplatforms have shown promise for glioma therapy, enabling targeted delivery under external field control.[43] Similarly, smart materials integrating diagnostic and therapeutic functions within a single system have been developed for enhanced tumor selectivity and real-time imaging.[44,45] While these approaches offer sophisticated control and versatility, they often require external stimuli (*e.g.*, magnetic fields, light), complex synthesis, or suffer from scalability and immunogenicity concerns. In contrast, HA NPs leverage the natural bone affinity of hydroxyapatite for passive bone targeting, which is particularly advantageous in the context of bone metastases, a scenario less frequently addressed by conventional tumor-targeting systems. Furthermore, selenium doping and Pt-functionalization allow for both redox-mediated activity and controlled cytotoxicity that does not rely on external triggers. This fully inorganic system ensures scalability, biocompatibility, and intrinsic bone selectivity, representing a complementary and more application-focused alternative to complex tumor-targeted nanocarriers, especially for bone-related malignancies. HA based nanostructures were synthesized *via* an aqueous precipitation method, which allows the formation of nanocrystalline HA NPs while ensuring charge balance in the reagent calculations.[28] Specifically, the substitution of a bivalent selenite anion (charge −2) in place of an orthophosphate anion (charge −3) generates a negatively charged vacancy (−1). This charge imbalance is compensated by the simultaneous release of one calcium cation and one hydroxyl anion.[28] Thus, the reagent quantities were determined based on the assumption that one orthophosphate ion and one calcium ion are replaced by a single selenite ion.

Comprehensive physico-chemical characterization of the resulting NPs was carried out, including size and morphology (TEM, SEM), elemental composition (SEM-EDX, ICP-AES),

colloidal stability (DLS, ζ-potential), and functional group analysis (ATR-FTIR).

TEM images (Fig. 1B1–B4) show that all synthesized NPs, including both undoped and Se-doped HA samples (2.5%, 5%, and 7.5%), predominantly appear elongated and rod-like in shape, with lamellar features (Fig. 1A1–A4). The NPs exhibit a marked tendency to form aggregates on TEM grids upon solvent evaporation, which makes an accurate determination of individual particle dimensions difficult, as single NPs are not always clearly distinguishable within the aggregates. For this reason, particle size is reported as a range, with average lengths in the interval of 30–60 nm for all samples.[46,47] SEM analysis performed on the same samples (Fig. 1C1–C4), probing the nanostructures at larger length scales, consistently confirms the overall morphology in good qualitative agreement with the TEM observations; however, at these observation scales, drying-induced aggregation of the NPs appears more evident. These morphological features are consistent with the size distribution and polydispersity index (PDI) values reported in Fig. 1D1–D4, as determined by DLS analysis. DLS measurements revealed a monomodal size distribution in suspension, indicating an overall good dimensional homogeneity of the nanostructures. A moderate increase in the average hydrodynamic diameter was observed for Se-doped HA compared to undoped HA; however, no clear trend with increasing Se content was detected. Such differences may be reasonably attributed to slight variations in a very limited degree of NP aggregation that may partially occur even when the NPs are well dispersed in suspension, rather than to a direct increase in primary particle size induced by Se doping. As previously reported,[32] the heterogeneous incorporation of selenite ions can induce subtle local lattice distortions and minor modifications in crystal growth dynamics, which may inhibit crystal growth while mildly favoring oriented aggregation, thereby only marginally influencing the hydrodynamic size measured by DLS. ζ-potential values of all HA dispersions were negative, reflecting the presence of surface phosphate and hydroxyl groups. Upon Se doping, a progressive decrease in the absolute ζ-potential was observed: -11.7 ± 0.3 mV for HASe2.5%, -10.1 ± 0.2 mV for HASe5%, and -9.8 ± 1.2 mV for HASe7.5%. This trend may be attributed to the incorporation of divalent selenite anions into the HA lattice, which induces a charge imbalance and compensatory structural rearrangements, ultimately resulting in a less negative net surface charge. A negatively charged HA surface is known to

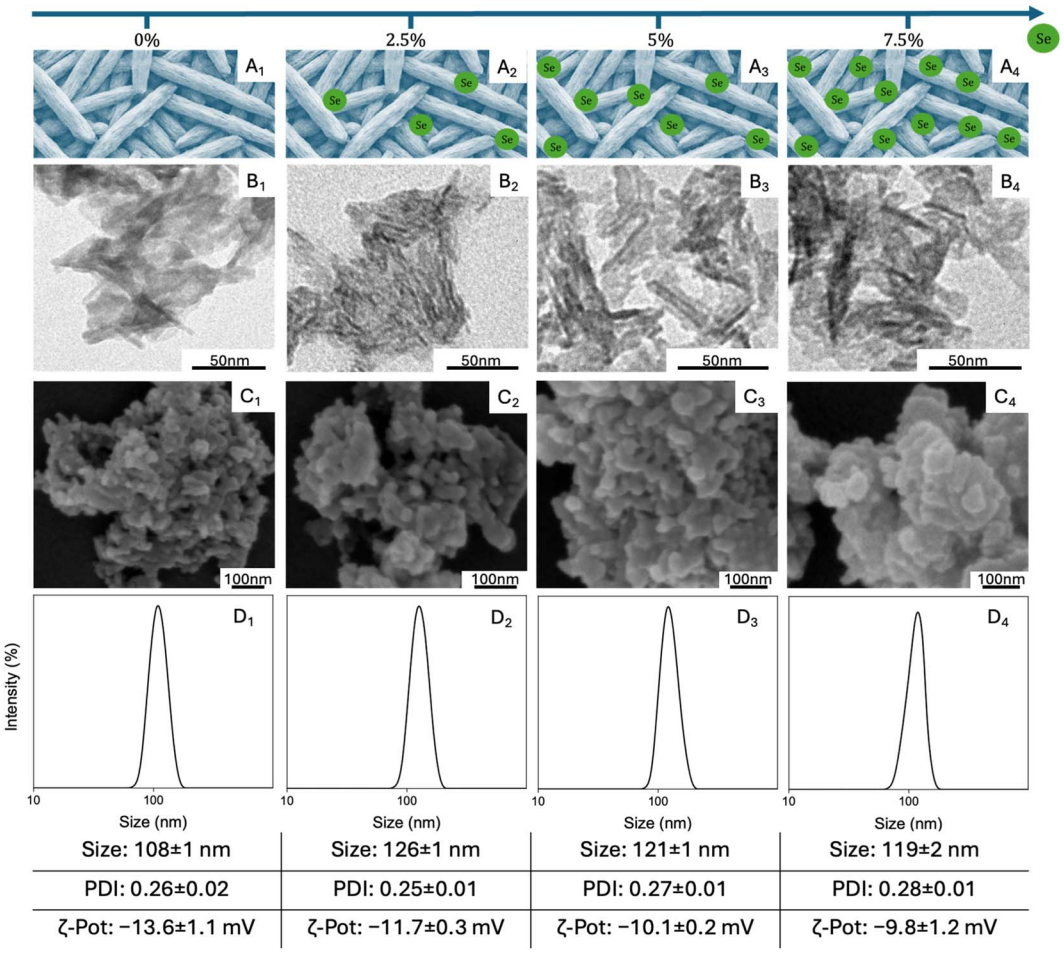

Fig. 1 (A) Schematic sketches (not drawn to scale), (B) TEM representative micrographs, (C) SEM representative micrographs (EHT = 5.00 kV, WD = 5.0 mm, aperture size = 30.00 μm, scale bar = 100 nm) and (D) DLS measurements of HA NPs (D1) in absence and (D2–D4) in presence of Se at different initial concentrations: 2.5, 5 and 7.5%. Table reporting the values of mean sizes, polydispersion index (PDI) and ζ-potential values.

promote interaction and adhesion with bone cells, which is advantageous for bone tissue engineering applications.[46,48]

Simultaneously with SEM imaging, EDX analysis confirmed the elemental composition of the samples, consistently detecting calcium (Ca), phosphorus (P), and oxygen (O) (Table S1, SI), with the additional identification of selenium (Se) in the doped samples. To ensure data comparability across the different compositions, SEM-EDX spectra were acquired from the same predefined area on each sample. A progressive increase in Se signal intensity was observed in proportion to the nominal Se content used during synthesis, supporting the successful incorporation of Se into the HA-based nanostructures.

Selected elemental composition (selenium, calcium, phosphorus) was also assessed by ICP-AES (Table 2). The Se content determined by both SEM-EDX and ICP-AES was comparable, although SEM-EDX slightly underestimated the absolute values due to its surface-limited and semi-quantitative nature. Nonetheless, both techniques consistently confirmed that Se incorporation into HA NPs was proportional to the nominal Se concentration used during synthesis (Fig. S1).

The bulk Ca/(P + Se) ratio was determined from the ICP-detected molar atomic percentage and range from about 1.58 in undoped HA to 1.43 in HASe7.5%. In line with previous observations on HASe with high Se concentrations, as reported by some of us,[32] the bulk Ca/(P + Se) ratio decreases as the Se substitution percentage increases. This could be attributed to the fact that the synthesis was performed under stoichiometric conditions, with a slight calcium deficiency imposed during the reaction.

FT-IR spectroscopy (Fig. S2) was performed to qualitatively confirm the Se substitution process. The results are consistent with previous findings,[32] considering the lower amount of sodium selenite used in this new synthesis. Briefly, the FT-IR spectra of HASe with reduced Se content showed the characteristic phosphate (PO_4^{3-}) vibration bands at ~1092, 1037, 603, and 567 cm^{-1}. The selenite (SeO_3^{2-}) bands were still present but as expected appear less intense compared to previous high-Se samples. Specifically, a weak band is observed around 750 cm^{-1}, attributed to Se–O vibrations resulting from selenite ion substitution in HA NPs. This band is shifted compared to free sodium selenite, likely due to changes in the counter-ion environment of the incorporated selenite. Unlike previous samples, no carbonate (CO_3^{2-}) bands were detected, indicating minimal or absent carbonate incorporation. Additionally, the broad band at ~3500 cm^{-1} and the peaks at 2500 and 1630 cm^{-1} correspond to the stretching and bending vibrations of water (H_2O) adsorbed on the nanocrystalline surface.

In vitro cytotoxicity of HASe NPs

The *in vitro* cytotoxicity of suspensions (0.003125, 0.00625, 0.0125, 0.025, 0.05, 0.1, and 0.2 mg mL^{-1}) of HA, HASe2.5%, HASe5.0%, and HASe7.5% was evaluated by assessing the viability of MCF7wt cancer cell line, after 72 h treatment, using the MTT assay (Fig. 2). The choice of testing the matrices on MCF7wt cells is justified by the fact that, although bone metastases can arise from almost all types of cancer, they most frequently originate from breast cancer cells.[49,50]

The MTT assay results for MCF7wt cells after 72 hours of direct exposure to NP suspensions revealed a dose-dependent decrease in cell viability across all tested samples, with Se concentrations ranging from 0.73 to 2.40 wt%. Pure HA NPs exhibited excellent cellular tolerance, showing only a modest reduction in viability across the tested concentration range. Cell viability remained above 65% even at the highest concentration tested (0.2 mg mL^{-1}), decreasing slightly from about 85% at 0.025 mg mL^{-1}. These findings indicate a minimal impact of HA NPs on cell viability and confirm their suitability as safe and biocompatible nanocarriers. In contrast, Se-doped HA samples (HASe2.5%, HASe5.0%, and HASe7.5%) showed a more pronounced cytotoxic effect even at higher concentrations. For HASe2.5%, cell viability decreased from about 80% at 0.025 mg mL^{-1} to nearly 30% at 0.2 mg mL^{-1}. A stronger cytotoxic effect was observed with increasing Se content. In fact, in HASe5.0%, viability fell from around 98% at the lowest concentration to approximately 20% at 0.2 mg mL^{-1}. A similar trend was observed with HASe7.5% except for the highest concentrations (0.1 and 0.2 mg mL^{-1}) where a very slight decrease in cytotoxicity was observed. This effect was probably due to a saturation effect caused by the high levels of selenium that entered tumor cells. Worth of note is also the fact that the Se content is rather similar in HASe5.0% and HASe7.5% (see Table 2). These results indicate that increasing Se content enhances the cytotoxic potential of the NPs, likely due to Se-induced alterations in cellular processes. The more significant reduction in viability at higher concentrations in Se-doped samples compared to pure HA suggests a potential role of Se in boosting the bioactivity of these NPs. However, HASe NPs with higher Se content (3.2 to 7.2 wt%) demonstrated strong cytotoxicity toward cancer cells but also caused increased toxicity in healthy cells.[32]

Table 2 Composition of HASe NPs (Se content%, bulk Ca/(P + Se) molar ratio. Values are reported as mean value ± SD, averaged out of at least three triplicates

Sample	Expected Se content (%wt)	Measured Se content[a] (%wt)	Measured Se content[b] (%wt)	Ca/(P + Se) molar ratio[b]
HA	0	0	0	1.58 ± 0.16
HASe2.5%	1.18	0.67 ± 0.05	0.73 ± 0.10	1.54 ± 0.14
HASe5.0%	2.37	1.57 ± 0.06	1.99 ± 0.15	1.47 ± 0.22
HASe7.5%	3.57	1.95 ± 0.06	2.4 ± 0.27	1.43 ± 0.35

[a] Calculated by EDX. [b] Calculated by ICP-AES.

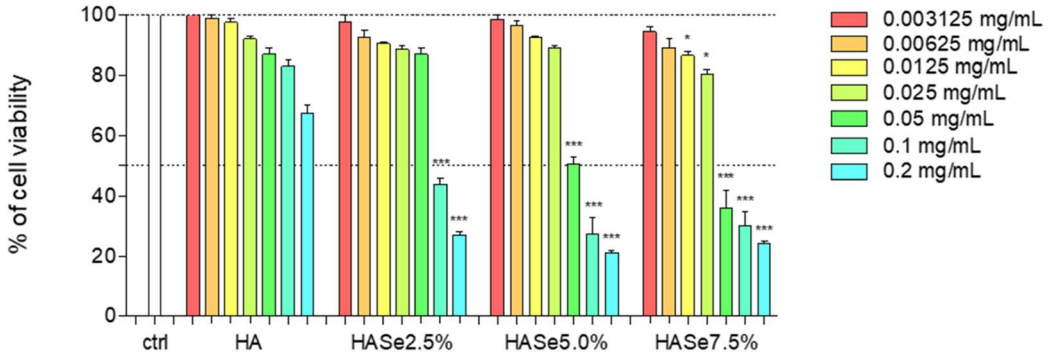

Fig. 2 Viability of MCF7wt cells after 72 hours of exposure to HA and HASe suspensions at different concentrations (0.003125–0.2 mg mL^{-1}). Each bar represents the mean ± SD of three experiments in triplicate: one-way ANOVA followed by Bonferroni's multiple comparison test *p < 0.05, **p < 0.01, ***p < 0.001 *vs.* HA at the same concentration.

Among the Se-doped NPs, HASe7.5% displayed one of the most pronounced antiproliferative effects, consistent with its higher Se content (2.4 wt% Se by ICP-AES). However, HASe7.5% was not selected for further functionalization. Instead, matrices with lower Se content, such as HASe5.0%, were selected as a strategic compromise between antiproliferative efficacy and potentially improved biocompatibility, in line with previous studies reporting toxicity concerns at elevated Se levels.[32] Although biocompatibility was not directly evaluated here on healthy cells, the selection was guided by the aim of minimizing systemic toxicity while maintaining relevant anticancer activity.

Loading of HA and HASe5.0% NPs with dinuclear Pt(II) complexes PtBP1 and PtBP2

Based on the *in vitro* cytotoxicity, HASe5.0% NPs were selected for loading of the two dinuclear Pt(II) bisphosphonate complexes (PtBPs), namely PtBP1 and PtBP2 (Fig. 3C and D), to achieve a combined and synergistic antitumor effect. The pure HA sample was included as a biocompatible reference matrix. The selection of PtBP1 was driven by the presence of the $[Pt(1R,2R\text{-DACH})]^{2+}$ residue, corresponding to the pharmacologically active moiety of the clinically used drug oxaliplatin. In contrast, PtBP2 contains an isomer of 1*R*,2*R*-DACH (*cis*-1,4-DACH), present in the complex known as kiteplatin ($[PtCl_2(cis\text{-}1,4\text{-DACH})]$), which has demonstrated the ability to overcome both the cisplatin and the oxaliplatin-resistance.[51] Previous studies showed that PtBP1 and PtBP2 exhibit significant *in vitro* cytotoxicity against four human tumor cell lines, with PtBP1 consistently more active than PtBP2 in all cell lines.[41] Moreover, both Pt(II) complexes displayed enhanced anticancer activity compared to oxaliplatin and free zoledronate in MCF7 wt and HepG2 cancer cell lines, outperforming the previously reported $[\{cis\text{-}Pt(NH_3)_2\}_2(ZL)]^+$,[40] which contains the platinum moiety present in clinically used cisplatin. Taken together, these findings underscored the therapeutic relevance of both PtBP1 and PtBP2 and provide a strong rationale for their further investigation in combination with HA/HASe-based materials to exploit potential synergistic antitumor effects.

Prior to PtBP1 and PtBP2 loading, HA and HASe5.0% NPs were characterized for their textural properties, since parameters such as surface area, pore volume and pore size distribution strongly influence cargo loading capacity, release behaviour and the stability of therapeutic agents incorporated within the materials. The textural properties of HA and HASe5.0% NPs were analysed by nitrogen adsorption analysis. The nitrogen adsorption–desorption isotherms were registered at 77 K (Fig. 3A); the specific surface area of the samples was evaluated with the Brunauer–Emmett–Teller (BET) model and the pore size distribution was evaluated through the Non-Local Density Functional Theory (NLDFT) (Fig. 3B). Both HA and HASe5.0% NPs exhibit type V isotherms, characterized by a sharp increase at high relative pressure, indicative of weak adsorbent–adsorbate interaction, typical of material containing large mesopores.[52] The incorporation of Se (HASe5.0%, blue curve) resulted in a higher volume of adsorbed nitrogen compared with pure HA NPs (green curve), indicating that Se substitution enhances the surface area, that changed from 150 ± 1 to 175 ± 1 $m^2\ g^{-1}$ for HA and HASe5.0% NPs, respectively. Moreover, HASe5.0% NPs displayed a small H1-type hysteresis loop, revealing the presence of a narrow mesopore size distribution.[52] The pore size distribution obtained from the NLDFT model is shown in Fig. 3B. Pure HA NPs exhibited a broad distribution, reflecting irregular porosity and poorly defined mesostructures, mainly attributable to interparticle voids. In contrast, the HASe5.0% profile showed a sharp and intense peak centered around ~25 nm, confirming the presence of a well-defined mesoporous structure. The total pore volume, calculated at relative pressure $p/p_0 = 0.99$, was 0.78 and 0.84 $cm^3\ g^{-1}$ for HA and HASe5.0% NPs, respectively, accounting also for interparticle porosity. Overall, these results demonstrate that Se substitution plays a crucial role in tailoring the textural properties of HA NPs, promoting the formation of a more organized mesoporous network with increased surface area and pore volume, and smaller pores, which can influence the loading efficiency.

Fig. 3F shows the loading percentage of PtBP1 and PtBP2 onto HA and HASe5.0% NPs. PtBP1 exhibited a higher loading on HA NPs (24.52%) compared to HASe5.0% (15.50%). A similar, but more pronounced, trend was observed for PtBP2, with an encapsulation efficiency of 14.65% on HA NPs and only

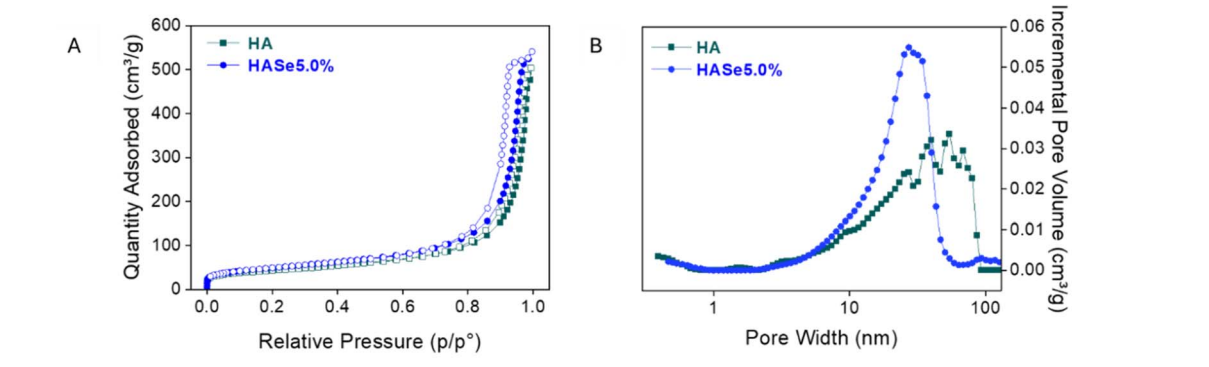

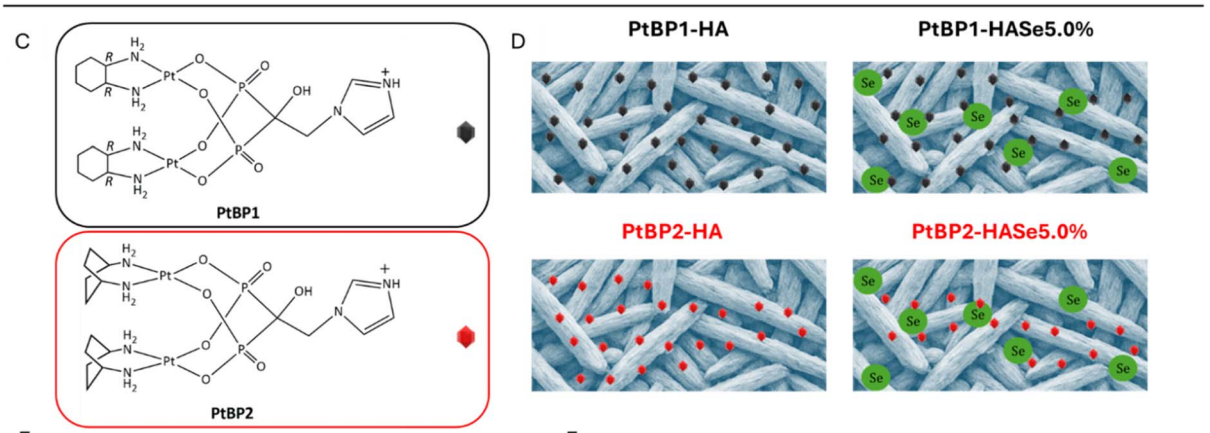

E

Samples	Measured Se content (%wt)	Measured Pt content (%wt)
HA	0	0
HASe5.0%	1.99 ± 0.15	0
PtBP1-HA	0	1.51 ± 0.07
PtBP2-HA	0	0.90 ± 0.03
PtBP1-HASe5.0%	0.23 ± 0.12	0.96 ±0.20
PtBP2-HASe5.0%	0.53 ± 0.20	0.35 ± 0.12

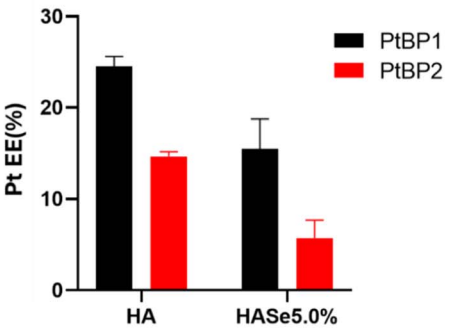

Fig. 3 (A) N_2 physisorption isotherms for the prepared samples, HA and HASe5.0% NPs (green curve and blue curve, respectively); (B) pore size distributions of HA and HASe5.0% NPs; (C) molecular structures of two dinuclear Pt(II) bisphosphonate complexes (PtBP1 in black and PtBP2 in red); (D) schematic sketches of HA and HASe5.0% NPs loaded with PtBP1 and PtBP2 (not drawn in scale); (E) table reporting the %wt of Se and Pt in HA and HASe5.0% before and after the loading process by ICP-AES; (F) encapsulation efficiency (EE%) of PtBP1 and PtBP2 on HA and HASe5.0% NPs.

5.72% on HASe5.0%. These results indicate a lower amount of PtBP2 loaded into HA compared to PtBP1. The lower encapsulation efficiency of PtBP2 may be attributed to the structural differences in the chelating diamine ligands. Although the bisphosphonate moiety is primarily responsible for binding to HA *via* calcium coordination as well as *via* interaction between the protonated imidazole ring and phosphate ions on the HA surface, the nature of the platinum-bound diamine influences the overall molecular geometry. In PtBP1, the 1*R*,2*R*-diaminocyclohexane ligand may allow a molecular conformation that better accommodates the spatial orientation of the bisphosphonate group for effective interaction with HA. In contrast, the *cis*-1,4-diaminocyclohexane in PtBP2 imposes a more rigid geometry and more distant coordination Pt-planes, which may reduce the accessibility or orientation of the bisphosphonate moiety toward the HA surface, thereby lowering the encapsulation efficiency. In addition to these structural considerations, textural differences between HA and HASe5.0% also contribute to the observed loading behaviour. As shown by the nitrogen adsorption–desorption analysis, Se substitution induces significant modifications in the mesoporous architecture, leading to a narrower pore size distribution and reduced average pore diameter compared to pure HA. Since larger mesopores can better accommodate the steric requirements of bulky PtBP complexes, the reduced pore dimensions in HASe5.0% likely impose spatial constraints that limit the

overall loading capacity of both PtBP1 and PtBP2. This structural effect, combined with the lower availability of Ca^{2+} ions caused by partial substitution with Se, aligns with previous observations reported by some of us regarding the adsorption of a Pt(II)-pyrophosphate compound, [Pt(dihydrogenpyrophosphate)(*cis*-1,4-DACH)], on HA and HASe NPs[39] and further explains the reduced encapsulation efficiency in Se-doped HA NPs. Additionally, ICP-AES analysis of the supernatants after the loading process confirmed a substantial release of Se from Se-doped HA (data not shown). Interestingly, a more pronounced Se release was detected for PtBP1-HASe5.0% compared to PtBP2-HASe5.0%, which was consistent with the greater reduction in Se%wt observed in PtBP2-loaded samples relative to those loaded with PtBP1 (Fig. 3E). While this may be partially explained by an increased dissolution of HASe nanocrystals induced by the adsorbed complex, it is also likely that the higher loading of PtBP1 is directly associated with a greater displacement or destabilization of Se within the HASe NPs In contrast, the lower loading of PtBP2 may have resulted in less interaction with the Se-doped HA structure, thereby leading to a reduced Se release Se (Fig. 3E). This suggests that the extent of PtBP adsorption/loading may directly influence the Se release, possibly due to competition for surface binding sites or perturbation of the Se-substituted region within the HASe structure. Consequently, the adsorption of PtBP1 onto HASe5.0% NPs led to a significant reduction in the Se content of the PtBPs-loaded Se-doped HA NPs (Fig. 3E).

The morphology of the HA and HASe5.0% after the PtBP1 and PtBP2 adsorption was also assessed by TEM characterization, resulting in no significant morphological changes in both NPs after PtBP1 and PtBP2 adsorption process. The HA NPs, in both cases and for both Pt-based complexes, retained their original structures, while a diffuse halo surrounding them, appeared, which can be attributed to the presence of an organic matrix related to the adsorption/loading process (Fig. 4).

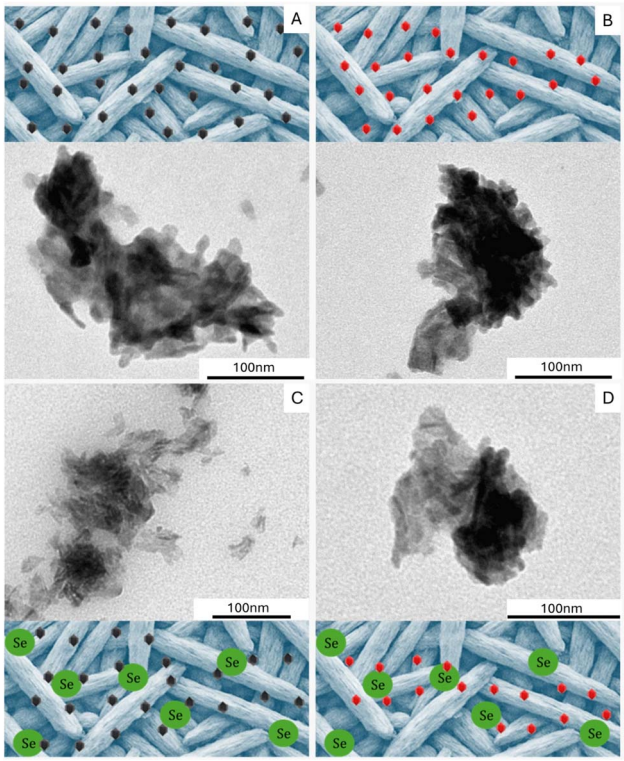

Fig. 4 Representative TEM micrographs of HA (A and B) and HASe5.0% (C and D) after loading with PtBP1 and PtBP2, respectively (scale bar 100 nm), along with the corresponding schematic sketches (not drawn in scale).

In vitro cytotoxicity of PtBP-HASe NPs

Following the selection of Se-doped HA matrices and their functionalization with platinum(II) complexes, the *in vitro* cytotoxic activity of the resulting HASePt NPs was assessed on MCF7wt breast cancer cells to evaluate the therapeutic potential of the combined Se–Pt system.

A direct comparison with empty HASe5.0% NPs is not suitable in terms of concentration, considering the significant release of Se observed after the adsorption process (Fig. 5). However, considering the %wt of Pt and Se in each sample, Fig. 5 highlights significant differences in cytotoxicity among HA, HASe5.0%, PtBP1-HA, PtBP2-HA, PtBP1-HASe5.0%, and PtBP2-HASe5.0%. For a direct comparison, the cell viability data of HA and HASe5% NPs without Pt-based complex loading (Fig. 2) are also reported in Fig. 5.

As described above, pure HA NPs exhibited low cytotoxicity, oppositely to HASe5.0% NPs that showed a strong cytotoxic effect, with viability sharply decreasing as concentration increased. When comparing the cytotoxic effect of PtBP1-HA and PtBP1-HASe5.0% NPs, this latter exhibited greater cytotoxicity, particularly at 0.2 mg mL^{-1}, where viability (*ca.* 45%) was lower than in PtBP1-HA NPs (*ca.* 51%). This trend suggests that the effect of reduced platinum content on the cytotoxicity (being higher in PtBP1-HA: 1.51 %wt *vs.* 0.96 %wt in PtBP1-HASe5.0%) is compensated for the presence of selenium that plays a key role in further reducing cell viability. Indeed, PtBP1-HASe5.0% contains Se (0.23%wt), which may enhance its biological effect compared to that of PtBP1-HA (Fig. 3E and 5). Comparison between HASe5.0% and PtBP1-HASe5.0% shows that at low concentrations platinum plays a key role in reducing cell viability while, the higher content in selenium of HASe5.0% (1.99 % wt; Table in Fig. 3E) as compared to PtBP1-HASe5.0% (0.23 %wt) seems to predominate at high concentrations. Further insights emerged when comparing the cytotoxic effects of the matrices with those of the two free PtBP complexes. Interestingly, as free compounds, PtBP1 showed higher cytotoxicity than PtBP2, probably because of the presence of the 1*R*,2*R*-diaminocyclohexane ligand in PtBP1, which may improve cellular uptake or DNA interaction.[41] However, once adsorbed on HA or HASe, this trend was reversed: PtBP2-HA and PtBP2-HASe5.0%, despite containing less Pt (0.90 and 0.35 wt%, respectively) than PtBP1-HA and PtBP1-HASe5.0% (1.51 and 0.96 wt%, respectively), demonstrated stronger cytotoxic effects (Fig. 3E and 5). This could be explained by differences in adsorption/loading behavior and matrix interaction. ICP-AES data showed that PtBP2 was adsorbed in lower amounts

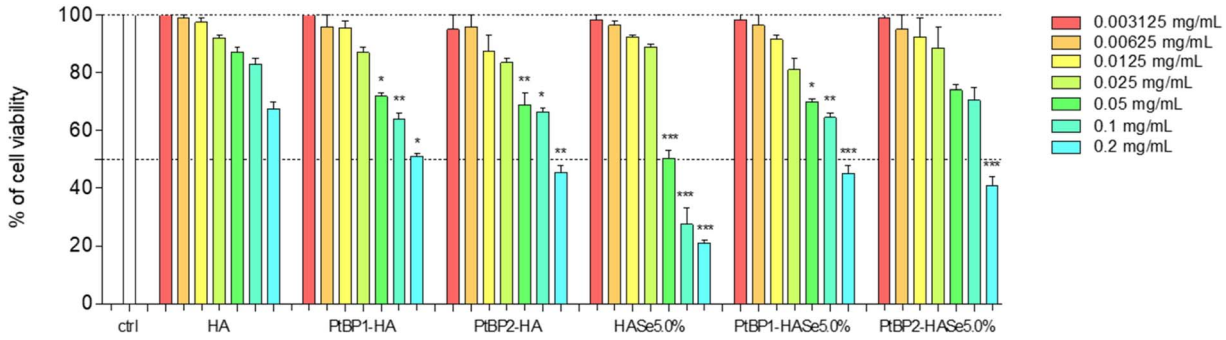

Fig. 5 Viability of MCF7wt cells after 72 hours of exposure to HA, PtBP-HA, HASe5.0%, and PtBP-HASe suspensions at different concentrations (0.003125–0.2 mg mL^{-1}). Each bar represents the mean ± SD of three experiments in triplicate: one-way ANOVA followed by Bonferroni's multiple comparison test *$p < 0.05$, **$p < 0.01$, ***$p < 0.001$ *vs.* HA at the same concentration.

compared to PtBP1 onto both HA and HASe matrices. This reduced binding efficiency, possibly due to the more rigid geometry of the *cis*-1,4-diaminocyclohexane ligand in PtBP2, may result in a looser association with the NP surface, facilitating a higher release rate of the active Pt species under biological conditions.

Finally, PtBP2-HASe5.0% demonstrated higher cytotoxicity than PtBP1-HASe5.0%, even though it contained less Pt (0.35 % wt *vs.* 0.96 %wt), again indicating that selenium plays a critical role in reducing cell viability. The presence of Se (0.23 %wt in PtBP1-HASe and 0.53 %wt in PtBP2-HASe) likely contributes to enhanced biological activity, even at relatively low concentrations (Fig. 3E and 5).

Overall, these results indicate that Pt-loaded HA NPs induce a controlled cytotoxic response, while even small amounts of Se significantly enhance this effect. The combined presence of Pt and Se in PtBP-HASe5.0% leads to stronger cytotoxicity than in PtBP-HA though still lower than HASe-5%. Since HASe NPs with higher Se content have been shown to induce strong cytotoxicity in cancer cells but also increased toxicity in healthy cells, the PtBP-HASe5.0% samples could represent a promising alternative. Their lower Se content might help balancing the potent anticancer effects while reducing the risk of excessive toxicity to healthy tissues, making these matrices promising candidates for further investigations.

Oxidative stress

To further elucidate the mechanisms underlying the cytotoxic effects observed for Se-doped and Pt-loaded HA NPs, we investigated the potential involvement of reactive oxygen species (ROS) in the antiproliferative response. Oxidative stress is a well-known contributor to cancer cell death, particularly through ROS-induced damage to cellular structures such as lipids, proteins, and DNA.[53]

Thus, the contribution of oxidative stress to the cytotoxic activity of platinum-bisphosphonate complexes (PtBP1 and PtBP2) was first assessed in MCF7wt cells after 48 hours of treatment with increasing doses ranging from 1.56 to 100 μM, by comparing cell viability in the presence or absence of the antioxidant α-tocopherol (Fig. 6). Both platinum complexes induced a dose-dependent decrease in MCF7wt cell viability, and in both cases, the co-treatment with α-tocopherol significantly rescued cell survival. This indicates that ROS generation plays a relevant role in their antiproliferative activity.

The protective effect of the antioxidant appeared more marked in cell treated with PtBP1, however both compounds likely rely on a combination of mechanisms, including oxidative stress and the well-established ability of platinum(II) complexes to form covalent adducts with DNA, interfering with transcription and replication processes.

To further contextualize these findings, the comparison with oxaliplatin and kiteplatin (Fig. S3) provides additional insight into the potential contribution of oxidative stress to the cytotoxicity of platinum-based compounds. Oxaliplatin, a clinically used drug that shares the same carrier ligand as PtBP1 (1*R*,2*R*-DACH), showed a notable rescue of cell viability in the presence of α-tocopherol, suggesting a possible role of ROS in its mechanism of action[54,55] in addition to DNA targeting.[56,57] Similarly, kiteplatin, a Pt(II) compound bearing the *cis*-1,4-DACH ligand present in PtBP2, also showed partial protection by α-tocopherol (Fig. S3). These findings further suggest that ROS generation contributes to cytotoxicity as an additional layer of activity, acting alongside the established DNA-binding pathway characteristic of platinum(II) compounds.

In contrast, sodium selenite (Fig. S3) also reduced cell viability in a dose-dependent manner, but the co-treatment with α-tocopherol resulted in only modest or inconsistent protection. This suggests a more complex mechanism of action, possibly involving both redox-dependent and redox-independent pathways. Selenium compounds are known for their dual antioxidant and pro-oxidant nature, and their biological effects are highly context-dependent, varying with dose, cell type, and redox status.[23,26] In particular, selenite can modulate cellular redox signaling, impair mitochondrial function, and interfere with thiol-containing proteins, mechanisms that may not be fully counteracted by classical antioxidants such as α-tocopherol.

The involvement of oxidative stress was finally investigated on the NPs (Fig. 7), at concentrations ranging from 0.05 to 0.2 mg mL^{-1}, after 48 hours of incubation. As expected, pure HA did not show significant sensitivity to α-tocopherol, confirming

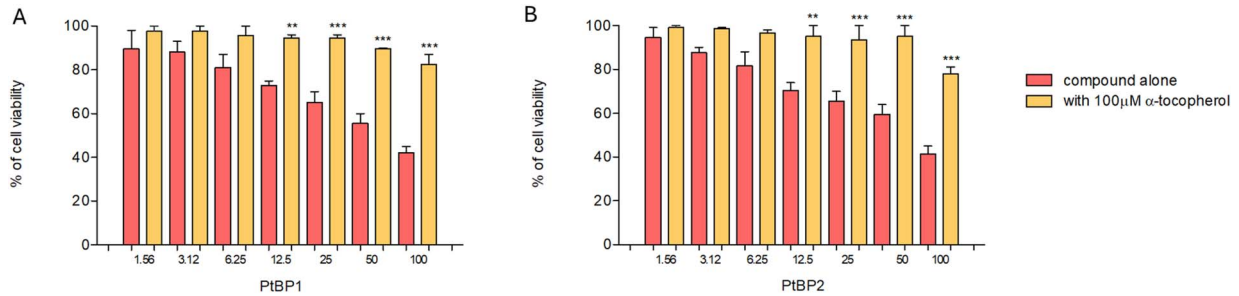

Fig. 6 Viability of MCF7wt cells after 48 hours of exposure to PtBP1 (A) and PtBP2 (B) at increasing concentrations (1.56–100 μM), in the presence or absence of the antioxidant α-tocopherol (100 μM). Cell viability was assessed by MTT assay. Each bar represents the mean ± SD of three experiments in triplicate: one-way ANOVA followed by Bonferroni's multiple comparison test *$p < 0.05$, **$p < 0.01$, ***$p < 0.001$ *vs.* respective test compound without 100 μM α-tocopherol.

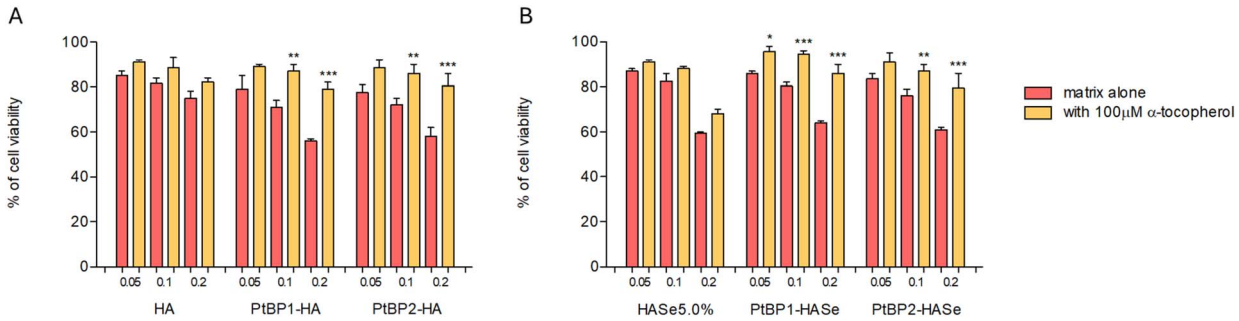

Fig. 7 Viability of MCF7wt cells after 48 hours of exposure to HA, PtBP1-HA, and PtBP2-HA (A) and to HASe5.0%, PtBP1-HASe5.0%, and PtBP2-HASe5.0% (B) suspensions at different concentrations (0.05, 0.1, and 0.2 mg mL^{-1}), in the presence or absence of the antioxidant α-tocopherol (100 μM). Cell viability was assessed by MTT assay. Each bar represents the mean ± SD of three experiments in triplicate: one-way ANOVA followed by Bonferroni's multiple comparison test *$p < 0.05$, **$p < 0.01$, ***$p < 0.001$ *vs.* respective test compound without 100 μM α-tocopherol.

its relevant degree of biocompatibility and absence of ROS-related mechanisms. Upon functionalization with platinum complexes, both PtBP1-HA and PtBP2-HA exhibited increased cytotoxicity that was partially reversed by α-tocopherol co-treatment, confirming that ROS contribute to their biological activity.

Interestingly, the HASe5.0% matrix alone (Fig. 7) did not respond to antioxidant treatment, indicating that its cytotoxic effect, while pronounced, is not primarily ROS-driven. This is consistent with the known complexity of selenite mechanisms, which involve mitochondrial impairment and redox imbalance that may not be neutralized by classical antioxidants. When Se-doped matrices were combined with Pt complexes, a protective effect of α-tocopherol was observed, similarly to what was seen with their HA-based counterparts. This suggests that ROS generation also contributes to the cytotoxicity of PtBP1-HASe5.0% and PtBP2-HASe5.0%. It is important to note that ROS involvement was assessed at 48 hours, while the cytotoxicity reported in Fig. 4 was evaluated at 72 hours. Therefore, although oxidative stress may participate in the mechanism of action, it is likely complemented by redox-independent processes, potentially influenced by the combined presence of platinum and selenium within the NP matrix.

Conclusions

Given the challenges associated with high Se content and its potential toxicity, the aim of this study is to explore a balance between therapeutic efficacy and potential biocompatibility. A series of Se-doped HA (HASe) NPs was synthesized, achieving effective Se substitution up to 2.40 wt%, significantly lower than the 13 wt% previously reported.[32] Physico-chemical analyses (TEM, FT-IR, EDX, ICP-AES) confirmed the successful incorporation of Se into the HA lattice. *In vitro* cell tests on MCF7wt showed a clear dose-dependent cytotoxicity of Se-doped HA NPs, with cell viability decreasing significantly as both Se content and NP concentration increased. In particular, HASe5.0% was identified as a lead material, showing a reduction in cell viability from ~98% to ~20% across the tested concentrations, while maintaining a lower Se content (1.99 wt%) compared to previously reported Se-doped matrices.[32] The adsorption of PtBP1 and PtBP2 onto HASe5.0% (PtBP-HASe) enhanced the cytotoxic effect when compared to PtBP-HA despite having a lower Pt content. Importantly, PtBP-HASe achieved a cytotoxic profile comparable to that of highly doped HASe (*e.g.*, HASe5.0%), but with significantly reduced Se content (0.23 and 0.53 wt% for PtBP1-HASe and PtBP2-HASe, respectively), potentially minimizing the adverse effects observed in healthy

cells. These results suggest that Se plays a critical role in enhancing the cytotoxic response, even at lower concentrations, and that the combined Pt/Se system offers a more potent anticancer activity than either element alone. In addition to cytotoxicity assessment, mechanistic investigations showed that reactive oxygen species contribute to the antiproliferative activity of both the platinum complexes and the functionalized NPs, providing insight into the redox-mediated cytotoxicity of these systems.

Overall, the PtBP-HASe formulation stands out as promising biomaterials for bone-targeted cancer therapy, capable of maximizing anticancer efficacy while potentially minimizing systemic toxicity. Although this study primarily focuses on the material's synthesis, characterization, and anticancer activity, future investigations will be necessary to further assess its effects on healthy cells and overall biocompatibility.

Author contributions

A. B.: writing – review & editing, writing – original draft, investigation, data curation. A. M. D. C.: writing – review & editing, investigation, data curation. F. R.: writing – review & editing, investigation, data curation. N. D.: writing – review & editing, investigation, data curation. R. C.: writing – review & editing, investigation, data curation. R. C.: writing – review & editing, investigation, data curation. E. F.: writing – review & editing, investigation, data curation. P. P.: writing – review & editing, investigation, data curation. C. P.: writing – review & editing, investigation, data curation. M. N.: writing – review & editing, supervision, methodology, investigation. N. M.: writing – review & editing, supervision, project administration, methodology, funding acquisition, data curation, conceptualization.

Conflicts of interest

There are no conflicts to declare.

Data availability

Some of the data supporting this article have been included as part of the supplementary information (SI). Other data are available upon request from the authors. Supplementary information: table S1, EDX analyses' data of HA, HASe2.5%, and HASe5.0%; Fig. S1, graph showing the correlation between the theoretical Se/(Se + P) ratio and the experimental Se content; Fig. S2, FTIR spectra of HASe samples; Fig. S3, viability of MCF7wt tumor cells after 48 h exposure to oxaliplatin, kiteplatin, and Na_2SeO_3 in the presence or absence of α-tocopherol (100 μM). See DOI: https://doi.org/10.1039/d5ra09348a.

Acknowledgements

We acknowledge financial support under the National Recovery and Resilience Plan (NRRP), Mission 4, Component 2, Investment 1.1, Call for tender No. 1409 published on 14.9.2022 by the Italian Ministry of University and Research (MUR), funded by the European Union – NextGenerationEU – Project Code P2022RLFZB, Title "Nanocrystalline Hydroxyapatite for the Local Delivery of Anticancer agents in the treatment of bone tumors and metastases" – CUP H53D23007980001 – Grant Assignment Decree No. 1384 adopted on 01/09/2023 by the Italian Ministry of Ministry of University and Research (MUR).

Notes and references

1 R. E. Coleman, *Clin. Cancer Res.*, 2006, **12**, 6243s–6249s.
2 D. Buenrostro, P. L. Mulcrone, P. Owens and J. A. Sterling, *Curr. Osteoporos. Rep.*, 2016, **14**, 151–158.
3 C. Criscitiello, G. Viale, L. Gelao, A. Esposito, M. De Laurentiis, S. De Placido, M. Santangelo, A. Goldhirsch and G. Curigliano, *Cancer Treat. Rev.*, 2015, **41**, 61–68.
4 S. Mercadante, *Pain*, 1997, **69**, 1–18.
5 S. Mercadante and F. Fulfaro, *Curr. Opin. Oncol.*, 2007, **19**, 308–314.
6 J. Nishida and T. Shimamura, *Med. Sci. Monit.*, 2008, **14**, RA107–RA113.
7 S. S. Syamchand and G. Sony, *Microchim. Acta*, 2015, **182**, 1567–1589.
8 S. H. Zhu, B. Y. Huang, K. C. Zhou, S. P. Huang, F. Liu, Y. M. Li, Z. G. Xue and Z. G. Long, *J. Nanoparticle Res.*, 2004, **6**, 307–311.
9 O. Geuli, N. Metoki, T. Zada, M. Reches, N. Eliaz and D. Mandler, *J. Mater. Chem. B*, 2017, **5**, 7819–7830.
10 Y.-H. Yang, C.-H. Liu, Y.-H. Liang, F.-H. Lin and K. C.-W. Wu, *J. Mater. Chem. B*, 2013, **1**, 2447.
11 W. Sun, J. Fan, S. Wang, Y. Kang, J. Du and X. Peng, *ACS Appl. Mater. Interfaces*, 2018, **10**, 7832–7840.
12 M. Zhang and K. Kataoka, *Nano Today*, 2009, **4**, 508–517.
13 M. Iafisco, M. Di Foggia, S. Bonora, M. Prat and N. Roveri, *Dalton Trans.*, 2011, **40**, 820–827.
14 M. Iafisco and N. Margiotta, *J. Inorg. Biochem.*, 2012, **117**, 237–247.
15 V. Sokolova and M. Epple, *Nanoscale*, 2011, **3**, 1957.
16 F. Rizzi, A. Panniello, R. Comparelli, I. Arduino, E. Fanizza, R. M. Iacobazzi, M. G. Perrone, M. Striccoli, M. L. Curri, A. Scilimati, N. Denora and N. Depalo, *Molecules*, 2024, **29**, 2367.
17 S. Lara-Ochoa, W. Ortega-Lara and C. E. Guerrero-Beltrán, *Pharmaceutics*, 2021, **13**, 1642.
18 H. Zhou and J. Lee, *Acta Biomater.*, 2011, **7**, 2769–2781.
19 D. Laurencin, N. Almora-Barrios, N. H. de Leeuw, C. Gervais, C. Bonhomme, F. Mauri, W. Chrzanowski, J. C. Knowles, R. J. Newport, A. Wong, Z. Gan and M. E. Smith, *Biomaterials*, 2011, **32**, 1826–1837.
20 Y. Li, Q. Li, S. Zhu, E. Luo, J. Li, G. Feng, Y. Liao and J. Hu, *Biomaterials*, 2010, **31**, 9006–9014.
21 H. R. Low, M. Avdeev, K. Ramesh and T. J. White, *Adv. Mater.*, 2012, **24**, 4175–4179.
22 J. M. Stolwijk, R. Garje, J. C. Sieren, G. R. Buettner and Y. Zakharia, *Antioxidants*, 2020, **9**, 420.
23 M. Kieliszek, B. Lipinski and S. Błażejak, *Cells*, 2017, **6**, 39.
24 H. W. Tan, Y.-M. Xu, D.-D. Wu and A. T. Y. Lau, *Expert Rev. Proteomics*, 2018, **15**, 113–130.

25 M. Enqvist, G. Nilsonne, O. Hammarfjord, R. P. A. Wallin, N. K. Björkström, M. Björnstedt, A. Hjerpe, H.-G. Ljunggren, K. Dobra, K.-J. Malmberg and M. Carlsten, *J. Immunol.*, 2011, **187**, 3546–3554.
26 B. Hu, R. Cheng, X. Gao, X. Pan, F. Kong, X. Liu, K. Xu and B. Tang, *ACS Appl. Mater. Interfaces*, 2018, **10**, 17345–17351.
27 K. Pajor, L. Pajchel, B. Kolodziejska and J. Kolmas, *Crystals*, 2018, **8**, 188.
28 J. Kolmas, E. Oledzka, M. Sobczak and G. Nałęcz-Jawecki, *Mater. Sci. Eng., C*, 2014, **39**, 134–142.
29 V. Uskoković, M. A. Iyer and V. M. Wu, *J. Mater. Chem. B*, 2017, **5**, 1430–1445.
30 Y. Wang, J. Ma, L. Zhou, J. Chen, Y. Liu, Z. Qiu and S. Zhang, *Interface Focus*, 2012, **2**, 378–386.
31 A. Barbanente, A. M. Di Cosola, L. Degli Esposti, M. Iafisco, M. Niso and N. Margiotta, *Materials*, 2025, **18**, 1043.
32 A. Barbanente, B. Palazzo, L. D. Esposti, A. Adamiano, M. Iafisco, N. Ditaranto, D. Migoni, F. Gervaso, R. Nadar, P. Ivanchenko, S. Leeuwenburgh and N. Margiotta, *J. Inorg. Biochem.*, 2021, **215**, 111334.
33 M. Freitas, V. Alves, A. B. Sarmento-Ribeiro and A. Mota-Pinto, *Biochem. Biophys. Res. Commun.*, 2011, **408**, 713–719.
34 C. P. Schroeder, E. M. Goeldner, K. Schulze-Forster, C. A. Eickhoff, P. Holtermann and H. Heidecke, *Biol. Trace Elem. Res.*, 2004, **99**, 017–026.
35 Y. J. Hu, Y. Chen, Y. Q. Zhang, M. Z. Zhou, X. M. Song, B. Z. Zhang, L. Luo, P. M. Xu, Y. N. Zhao, Y. B. Zhao and G. Cheng, *Biol. Trace Elem. Res.*, 1997, **56**, 331–341.
36 A. Ghorbani, B. Omidvar and A. Parsi, *J. Nephropathol.*, 2013, **2**, 129–134.
37 J. Zhang, D. Peng, H. Lu and Q. Liu, *Toxicol. Appl. Pharmacol.*, 2008, **226**, 251–259.
38 Q. Liu, X. Wang, X. Yang, X. Liang and Z. Guo, *J. Inorg. Biochem.*, 2010, **104**, 1178–1184.
39 A. Barbanente, R. A. Nadar, L. D. Esposti, B. Palazzo, M. Iafisco, J. J. J. P. Van Den Beucken, S. C. G. Leeuwenburgh and N. Margiotta, *J. Mater. Chem. B*, 2020, **8**, 2792–2804.
40 A. Barbanente, N. Ditaranto, A. Laghezza, P. Tortorella, F. P. Intini, C. Pacifico, G. Natile and N. Margiotta, *Dalton Trans.*, 2023, **52**, 6117–6128.
41 A. Barbanente, A. M. Di Cosola, M. Niso, L. D'Anna, S. Rubino, S. Indelicato, C. Pacifico, A. Terenzi and N. Margiotta, *J. Inorg. Biochem.*, 2025, **270**, 112916.
42 T. Latronico, F. Rizzi, A. Panniello, V. Laquintana, I. Arduino, N. Denora, E. Fanizza, S. Milella, C. M. Mastroianni, M. Striccoli, M. L. Curri, G. M. Liuzzi and N. Depalo, *ACS Chem. Neurosci.*, 2021, **12**, 4286–4301.
43 Z. Jiang, H. Zhang, W. Zhang, Y. Zhang, Y. Cui, L. Mei and Q. Wang, *Nano Today*, 2024, **56**, 102295.
44 Z. Wang, S. Liu, R. Ming, W. Wang, C. Wang, C. Li, J. Yang, F. Zhang, G. Lu, L. Mei and L.-L. Huang, *J. Control. Release*, 2025, **378**, 416–427.
45 N. P. Kar, J. Lin, A. HassankhaniRad, W. Li, A. R. Aboushanab, Y. Li and J. Sun, *Smart Mater. Med.*, 2025, **6**, 368–386.
46 A. L. C. Maia, C. H. Cavalcante, M. G. F. de Souza, C. de A. Ferreira, D. Rubello, S. Chondrogiannis, V. N. Cardoso, G. A. Ramaldes, A. L. B. de Barros and D. C. F. Soares, *Nucl. Med. Commun.*, 2016, **37**, 775–782.
47 M. Mir, F. L. Leite, P. S. de P. Herrmann Junior, F. L. Pissetti, A. M. Rossi, E. L. Moreira and Y. P. Mascarenhas, *Mater. Res.*, 2012, **15**, 622–627.
48 M. . Ferraz, F. . Monteiro, A. . Serro, B. Saramago, I. . Gibson and J. . Santos, *Biomaterials*, 2001, **22**, 3105–3112.
49 L. Thibaudeau, V. M. Quent, B. M. Holzapfel, A. V Taubenberger, M. Straub and D. W. Hutmacher, *Cancer Metastasis Rev.*, 2014, **33**, 721–735.
50 M. van Driel and J. P. T. M. van Leeuwen, *Arch. Biochem. Biophys.*, 2014, **561**, 159–166.
51 S. Savino, V. Gandin, J. D. Hoeschele, C. Marzano, G. Natile and N. Margiotta, *Dalton Trans.*, 2018, **47**, 7144–7158.
52 M. Thommes, K. Kaneko, A. V. Neimark, J. P. Olivier, F. Rodriguez-Reinoso, J. Rouquerol and K. S. W. Sing, *Pure Appl. Chem.*, 2015, **87**, 1051–1069.
53 Y. Zhao, X. Ye, Z. Xiong, A. Ihsan, I. Ares, M. Martínez, B. Lopez-Torres, M.-R. Martínez-Larrañaga, A. Anadón, X. Wang and M.-A. Martínez, *Metabolites*, 2023, **13**, 796.
54 H. Huang, O. Aladelokun, T. Ideta, C. Giardina, L. M. Ellis and D. W. Rosenberg, *Sci. Rep.*, 2019, **9**, 4954.
55 H. Tabassum, M. Waseem, S. Parvez and M. I. Qureshi, *Arch. Med. Res.*, 2015, **46**, 597–603.
56 T. Alcindor and N. Beauger, *Curr. Oncol.*, 2011, **18**, 18–25.
57 B. Ray, B. Gupta and R. Mehrotra, *J. Biomol. Struct. Dyn.*, 2019, **37**, 3838–3847.